IEEE Access
Multidisciplinary | Rapid Review | Open Access Journal

Received 5 April 2024, accepted 3 May 2024, date of publication 8 May 2024, date of current version 15 May 2024.

Digital Object Identifier 10.1109/ACCESS.2024.3398537

RESEARCH ARTICLE

Fractal Metamaterial Surfaces for UHF Sensing Applications

FRANCESCA VENNERI, (Member, IEEE), SANDRA COSTANZO, (Senior Member, IEEE), ANTONIO BORGIA, (Member, IEEE), AND GIOVANNI BUONANNO, (Member, IEEE)
DIMES, Università della Calabria, 87036 Arcavacata di Rende, Italy

Corresponding author: Francesca Venneri (venneri@dimes.unical.it)

This work was supported in part by the Ministero dell'Università e della Ricerca (MUR), Italy, and in part by the Programma Operativo Nazionale (PON) Ricerca e Innovazione (2014–2020)–Area di Specializzazione AEROSPAZIO, through the Project "Monitoraggio coltivazioni e zone marine costiere: Tecnologie satellitari di nuova generazione (OCEANOS)."

ABSTRACT A dual-band fractal metamaterial absorber is proposed as a promising alternative for sensing applications. A preliminary prototype, useful to validate the proposed configuration, is designed to operate in the Ultra-High Frequency (UHF) range. The inherent miniaturization skills of fractal geometries are effectively exploited to design and fabricate multiband/broadband absorbers with a small lattice size ($\leq \lambda_0/2$ at the smaller operating frequency f_0) and a very thin profile ($\leq \lambda_0/100$). Two pairs of Minkowski fractal patches, alternately arranged in four different quadrants and properly sized to achieve two distinct absorption peaks, are assumed for the absorber-sensor configuration. In the framework of dielectric material diagnostics, the MA structure shows an average relative sensitivity of 4.6% and a quality factor equal to 36. Very high absorption peaks (>99%) and quite good stable absorption rates versus incidence angle variations ($\geq$ 90% for TE polarization and $\geq$ 97% for TM polarization at both frequencies) are demonstrated both numerically and through experimental validations, thus proving the applicability of the proposed absorber sensor in low-frequency sensing applications.

INDEX TERMS Dual-band, fractals, metamaterial absorbers, microwave sensors.

I. INTRODUCTION

Metamaterial absorbers (MAs) are artificial structures, designed to detect and minimize the magnitude of the signal scattered by an object, due to an incident wave operating at a given frequency of the electromagnetic (EM) spectrum. They consist of a periodic arrangement of metallic patches printed on a thin and low-loss grounded dielectric sheet [1], [2]. The metallic pattern is properly shaped to realize perfect absorption at one or more given frequencies and/or within a desired frequency band. The MA concept is currently used in many applications throughout the EM-spectrum [2], [3], such as multipath reduction for indoor wireless systems, improvement of electromagnetic compatibility (EMC) performance of electronic products, reduction of radar signatures of targets. Unlike traditional microwave absorbers, such as $\lambda/4$-thick Salisbury screens, wedge-shaped anechoic panels and ferrite-based absorbers, MAs offer smaller footprints and lower weights, thus providing a promising and attractive alternative for those radio frequency (RF) applications using lower microwave frequencies ($\leq$3 gigahertz (GHz)). MAs have been intensively adopted for designing low frequency absorbing panels [4], [5], [6], [7], [8], [9], [10], useful: to avoid incorrect readings of Ultra-High Frequency Radio-Frequency IDentification (UHF-RFID) sensors [4], [5], [6], [7]; for EMC and noise reduction at Global System for Mobile communications (GSM) frequencies [8]; for RF energy harvesting within the GSM, Worldwide Interoperability for Microwave Access (WiMAX), Wireless Local Area Network (WLAN) and Industrial, Scientific and Medical (ISM) bands [9], [10].

As recently demonstrated in [11], [12], [13], and [14], MAs have the potential to develop innovative sensing devices in the microwave band. Indeed, the high frequency selectivity exhibited by microwave metamaterial absorbers allows to detect and discriminate the variation of environmental parameters [11], such as temperature and humidity, as well as physical and electrical properties of different materials, such as permittivity and density [14]. Furthermore, the design of

The associate editor coordinating the review of this manuscript and approving it for publication was Luyu Zhao.

© 2024 The Authors. This work is licensed under a Creative Commons Attribution-NonCommercial-NoDerivatives 4.0 License.
For more information, see https://creativecommons.org/licenses/by-nc-nd/4.0/

tunable and multifunctional two- or three-dimensional metastructures (MSs), is currently a trend in the terahertz (THz) range [15], [16], [17]. For example, a tunable multifunctional MS with polarization conversion (PC) and wave absorption functions is proposed in [15], based on the phase transition properties of vanadium dioxide (VO_2). A MS device capable of realizing PC and absorption function switching in the THz range is proposed in [16], based on the photoconductivity effect.

Miniaturization is a crucial factor in the development and use of MAs for sensing applications. It enables the manipulation of electromagnetic properties at smaller scales, resulting in MAs with enhanced absorption properties [18]. Miniaturized MAs can be integrated into compact devices and systems without compromising performance. This is particularly important in space-constrained applications such as electronics, telecommunications, and medical imaging. Fractal geometries have recently been investigated in these areas for their unique advantages in miniaturization [7], [19], [20], [21], [22], [23]. Fractal shapes exhibit self-similarity at different scales and space-filling properties, allowing the creation of complex structures with reduced size [24], [25]. These properties enable the creation of compact MAs that utilize the available space effectively, making them suitable for integration into small devices and systems. To the best of our knowledge, only a few studies [26], [27], [28] have employed fractal MAs to develop sensors with high absorption capacity while minimizing their physical footprint. Research should continue to explore new designs in the field of fractal MAs in order to exploit their full potential.

This work aims to contribute to this goal by proposing a fractal-based MA structure that shows promising high applicability in sensing with a significant level of miniaturization (up to 67% with respect to standard configurations, see section II-A), while maintaining good sensitivity. The design of a multi-band and ultra-thin fractal MA, which was preliminarily introduced by the authors in [29] for multipath mitigation within the UHF band, is discussed in detail and proposed for sensing applications in the framework of material diagnostics applications. The miniaturization skills of the adopted fractal shape are exploited to realize a dual-band operation mode, by properly fitting two or more small metallic patches inside the same MA-cell. Multi-band sensors are commonly used to enhance detection capabilities. They are useful in many practical applications that require multi-band sensing, such as facilitating multi-channel measurements or performing dielectric characterization of materials at different frequencies in a single step.

Despite other multi-band MAs presented in the literature [9], [10], [30], [31], [32], [33], [34], [35], [36], [37], [38], and [39], the proposed fractal MA allows to achieve very close absorption peaks (i.e., a frequency separation of about 80 megahertz (MHz)), by adopting a single layer structure with a very small thickness ($\leq \lambda_0/100$). In contrast, the MAs proposed in [9], [10], [30], [31], [32], [33], [34], [35], [36], [37], and [38] exhibit two or three absorption peaks, with a minimum frequency separation ranging from 430 MHz up to 4.85GHz. Furthermore, the MA cells suggested in [10], [30], [31], [32], [33], [34], [35], [36], [38], [39], [40], [41], [42], [43], and [44] have thicker profiles, ranging from $\lambda_0/76$ up to $\lambda_0/9$ at the lower absorbing frequencies.

The proposed MA structure also exhibits polarization-insensitive absorption behavior, very high angular stability and frequency scalability. Furthermore, depending on the frequency bands to be utilized, it can be readily fabricated using well-established techniques such as PCB milling, lithography or laser printing, showing high feasibility.

The sensing capability of the proposed MA-based sensor is numerically demonstrated by detecting the frequency shift of its absorption peaks caused by changes in the dielectric constant values of the sample under test (SUT). Compared to other frequency-variable planar sensors [39], [42], [45], [46], [47], [48], this sensor achieves a higher average relative sensitivity of about 4.6%. Furthermore, it offers a good trade-off between sensitivity, quality factor (Q), and unit cell size when compared to other MA-based sensors [45], [46], [47], [49], [50].

An 81-cell MA panel operating in the UHF frequency range is fabricated and tested using a far-field measurement setup consisting of a pair of transmit and receive horn antennas and a vector network analyzer. The measurements show very high absorption rates (>99%) and quite good angular stability at 878 MHz and 956 MHz. Finally, the sensing capabilities of the MA sensor are experimentally validated using a monostatic measurement setup to measure frequency variations in the panel reflection (i.e. absorption) response for different SUTs.

Future developments will aim to improve sensor sensitivity and integrate increasingly miniaturized MA-based sensors with reconfigurable materials or devices, such as PIN and liquid crystal diodes (LCDs), in order to provide multifunctional behavior with switchable functions. These techniques could include absorption/polarization conversion [16] and frequency-tunable operation [51] to enhance sensing performance and broaden the range of applications, particularly in the fields of environmental monitoring and biomedical research.

II. FRACTAL MA UNIT CELL GEOMETRY AND DESIGN

The proposed dual-band MA is shown in Figure 1. It comprises a frequency selective surface (FSS) consisting of a fractal periodic pattern of copper with a thickness of 35μm (the solid black part in Fig. 1(b)) printed on a grounded dielectric slab (the grey part in Fig. 1).

The layout of the proposed dual-band unit cell is depicted in Fig. 1(c), which considers two pairs of identical Minkowski patches, each designed to operate at a specific resonant frequency. The MA surface is illuminated by a plane wave with TE polarization and an angle of incidence equal to $(\theta_{inc}, \varphi_{inc}) = (0°,0°)$. The performance of the structure is then analyzed in the following sections by varying the characteristics of the incident plane wave (see Section II-B).

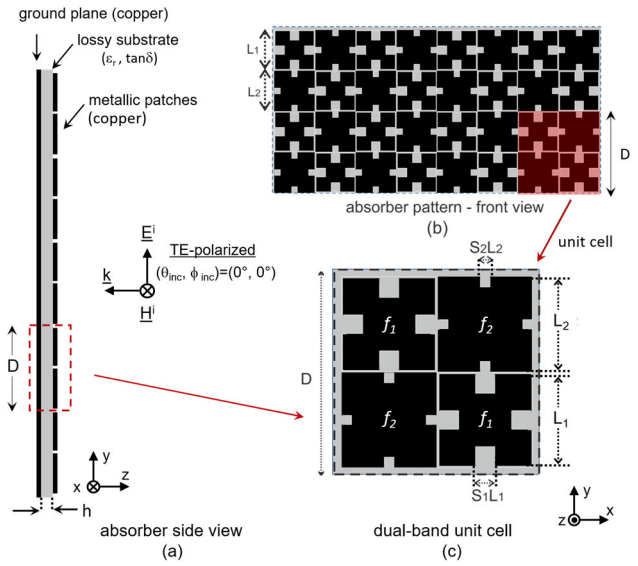

FIGURE 1. Fractal MA sensor: (a) side view; (b) front view; (c) unit cell.

The size of the Minkowski patches is properly adjusted to achieve complete absorption of the incident signal at the desired frequencies f_1 and f_2.

The theoretical absorptivity of a common MA structure can be calculated using the following formula:

$$\mathrm{A}(f) = 1 - |\Gamma(f)|^2 - |\mathrm{T}(f)|^2 . \tag{1}$$

The terms $\Gamma(f)$ and $\mathrm{T}(f)$ represent the reflection and transmission coefficients of the MA unit cell, respectively.

The operating principle of MAs is based on resonance phenomena. To achieve the maximum absorptivity in expression (1), both the resonance and matching conditions must be met at the chosen operating frequency f_0. This requires that the unit cell impedance $Z_{cell}(f_0)$ equals the free space impedance $\xi_0 = 377\Omega$. As a result, the reflection coefficient of the MA unit cell approaches zero, as shown in the following expression:

$$\Gamma(f_0) = \frac{Z_{cell}(f_0) - \xi_0}{Z_{cell}(f_0) + \xi_0} \cong 0 \tag{2}$$

In addition, the copper layer located at the rear of the MA cell, referred to as the ground plane in Fig. 1(a), prevents the transmission of the incident wave, resulting in a transmission coefficient of $\mathrm{T}(f) = 0$. Therefore, complete absorption of the incident EM energy is achieved at resonance, and the function (1) is maximized, i.e. $\mathrm{A}(f_0) \cong 1$. The absorption mechanism of MAs can be optimized and customized by selecting the appropriate substrate properties, such as permittivity (ε_r), loss tangent (tanδ) and thickness (h) and tuning the size/shape of the metallic pattern. Moreover, the absorption coefficient of MAs can be enhanced by replacing the metal pattern with a resistive paint or by incorporating lumped resistors [52]. Substrate effects can also be controlled by adjusting the free electronic charges present on the surface [53]. These latter methods may be advantageous for miniaturization, but they may result in more complex structures [52].

The design process and miniaturization capabilities of the proposed MA unit cell are described in detail below. Specifically, this section is divided into subsections that examine the design of single-band unit cells and their miniaturization effects compared to standard square-based cells; the design of a dual-band cell, an extensive analysis of its performance and explanation of the associated physical mechanisms; the potentialities and applications of the proposed fractal unit cell, and finally its frequency scalability.

A. SINGLE-BAND MA UNIT CELL DESIGN AND CONSIDERATIONS

The Minkowski fractal geometry, already proposed by the authors in [7] and [54], consists of an L × L square metal patch, suitably modified by removing a smaller SL × SL square from the center of its sides (Fig. 2), where S is a scaling factor ranging from zero to 1/3. The adopted fractal configuration allows to fit electrically longer resonators in smaller cells [54], [55], offering very interesting miniaturization possibilities. Indeed, it is well known that the resonant frequency f_0 of a metallic patch is inversely proportional to its effective electrical side length L_e (i.e., $f_0 \sim 1/L_e$), which in the case of the fractal patch in Fig. 2 is approximately equal to $L_e \cong (1 + 2S)\,L$ [7].

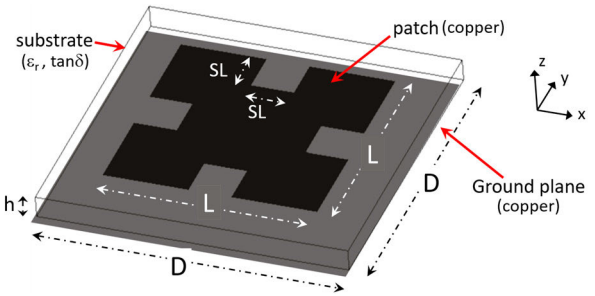

FIGURE 2. Single-frequency unit cell based on the Minkowski fractal shape.

Accordingly, the combined use of a shorter patch length L and a higher S value allows the resonant frequency f_0 to remain unchanged, while saving the occupied area in the cell. Furthermore, the Minkowski geometry provides two different degrees of freedom to achieve the perfect absorption condition at the desired resonant frequency f_0. In other words, both L and S can be used to match the MA unit cell impedance, Z_{cell}, to the free-space impedance $\xi_0 = 377\ \Omega$ at f_0 (i.e., $|\Gamma(f_0)| = \left|\frac{Z_{cell}(f_0)-\xi_0}{Z_{cell}(f_0)+\xi_0}\right| \cong 0 \Rightarrow \mathrm{A}(f_0) \cong 1$).

In order to prove the above statements, a set of fractal MA cells is designed at 878 MHz, characterized by a progressively smaller dimension D ranging from $0.3\lambda_0$ to $0.15\lambda_0$ (λ_0 is the free-space wavelength at f_0). A substrate with a thickness h equal to 3.2mm, a relative permittivity $\varepsilon_r = 4.2$ and a loss tangent $\tan\delta = 0.015$ is considered.

A commercial full-wave code is employed, using the infinite array approach [56] and assuming a normal incident plane wave. Fig. 3 depicts the simulated absorption and reflection coefficients (Fig. 3(b)) of the designed MA cells. They show that it is always possible to guarantee the maximum absorption condition at f_0 by an appropriate choice of L and S. In fact, although the use of a smaller cell size D forces the use of patches with a shorter length L (Fig. 3(a)), which would inevitably raise the resonance frequency, an appropriate increment of the S-factor allows to increase the electrical length of the patch, keeping the desired operating frequency ($f_0 = 878$MHz) and the corresponding matching condition unchanged (Fig. 3(b)).

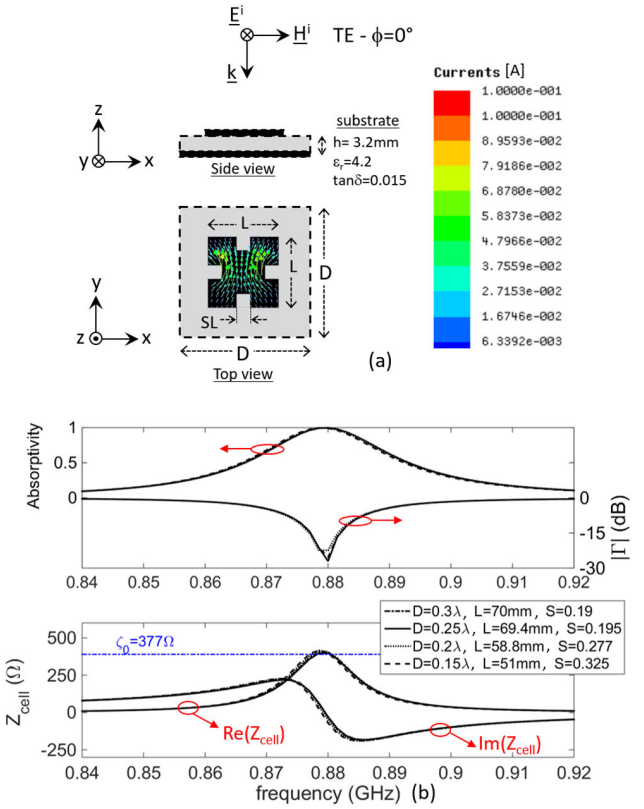

FIGURE 3. Single-frequency fractal-based unit cell: (a) current on the patch surface @ 878 GHz (D = 0.3λ, L = 70mm, S = 0.19); (b) reflection/absorption coefficient and unit cell input impedance vs. frequency for different cell sizes D.

The proposed fractal geometry allows for the design of more compact unit cells due to the fact that the current path on the fractal patch is curved close to the SL slits, extending the effective resonance length of the patch. This result is supported by physical evidence shown in Fig. 3(a).

In order to better appreciate the miniaturization capabilities of the proposed configuration, the above results are compared with the behavior of a standard square patch, printed on the same substrate. Fig. 4 shows the simulated absorption and reflection coefficients (Fig. 4(b)) of a set of square patch-based MA cells designed to work at 878 MHz and characterized by a progressively smaller dimension D ranging from $0.45\lambda_0$ to $0.25\lambda_0$. In particular, it can be observed from Fig. 4(b) that for smaller cell sizes ($D \leq 0.3\,\lambda_0$), the higher capacitive coupling between adjacent patches (see [7], [57] for more details) leads to very high resonant input impedances, causing a progressive mismatch and hence a reduction in the MA absorptivity. Therefore, for smaller unit cells and a fixed substrate layer, it is not always possible to optimize the square patch for maximum absorption. This is due to the fact that the synthesis of a square-based MA-cell is based on the use of only one degree of freedom, i.e. the patch length L, which is typically chosen to fix the unit cell resonance at the operating frequency f_0.Unlike the fractal patch, there is no further degree of control to adjust the real part of the unit cell impedance and thus the matching condition. In conclusion, comparing the results obtained for the fractal-based MA cell in Fig. 3 with those of the square-patch cell (Fig. 4), a 67% reduction in unit cell size can be appreciated.

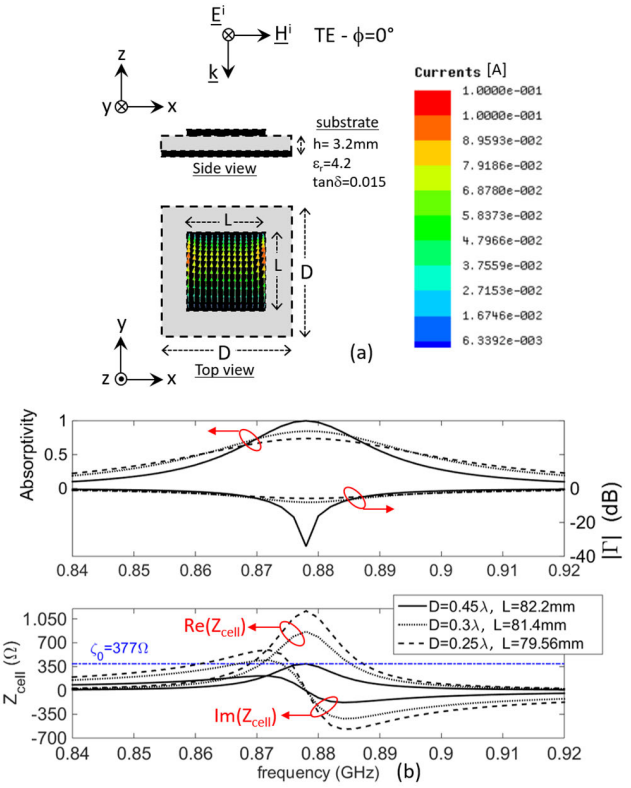

FIGURE 4. Single-frequency square-based unit cell: (a) current on the patch surface @ 878 GHz (D = 0.3λ, L = 81.4mm); (b) reflection/absorption coefficient and unit cell input impedance vs. frequency for different cell sizes D.

As a further analysis, the effects of substrate losses are considered in Fig. 5. Similar behavior can be observed for all designed fractal unit cells. In particular, Fig. 5(a) shows that the unit cell impedance Z_{cell} decreases from 1.2 kΩ down to 83Ω as the dielectric loss tangent, tanδ, increases from 0.005 up to 0.075, for a fixed permittivity $\varepsilon_r = 4.2$.

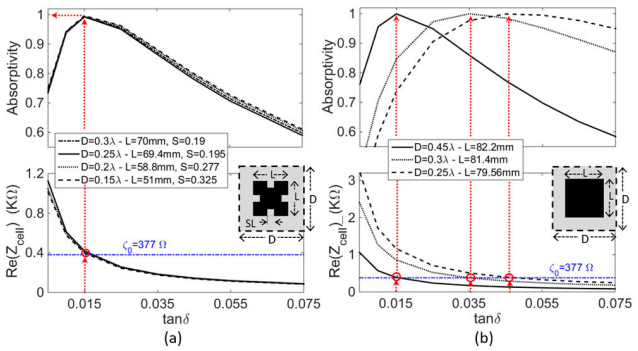

FIGURE 5. Absorption coefficient and unit cell input impedance vs. tanδ @ 878 GHz for different cell sizes D: (a) fractal-based unit cell; (b) square-based unit cell.

Therefore, if the value of tanδ differs from the one chosen during the design stage (i.e. tan$\delta = 0.015$ of Fig. 3), a mismatch occurs in the unit cell impedance, resulting in a reduction of the MA absorptivity (Fig. 5(a)) [57].

Hence, the use of a substrate with a higher loss tangent can be advantageous for enabling the miniaturization of the square-based unit cells depicted in Fig. 4. Figure 5(b) demonstrates that the perfect absorption condition can be achieved even with smaller D-size cells by using dielectric substrates with higher loss tangent. However, it is important to note that some of the conditions shown in the figure may not be physically feasible, as the loss tangent of the most commonly used printed circuit board (PCB) materials ranges from 0.025 to 0.001. Therefore, it can be confirmed that the proposed fractal patches shown in Figs. 4 and 5(a) are more suitable for designing miniaturized MA cells with a size of $D < 0.3\lambda_0$.

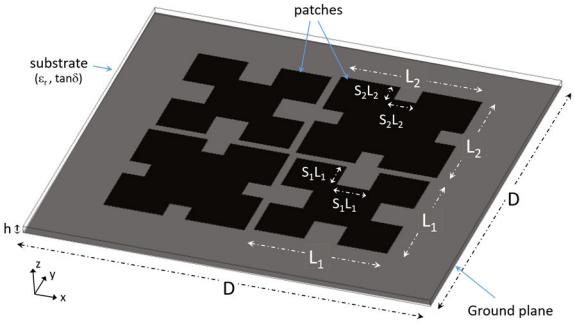

FIGURE 6. Dual-frequency unit cell based on the Minkowski fractal shape.

B. DUAL-BAND MA UNIT CELL DESIGN AND ANALYSIS

A dual resonant $0.4\lambda_0 \times 0.4\lambda_0$ cell is synthesized using the layout depicted in Fig. 6. Here, λ_0 represents the free space wavelength calculated at the lower operating frequency. A standard fiberglass laminate ($\varepsilon_r = 4.2$, tan$\delta = 0.015$, $h = 3.2\text{mm} \leq \lambda_0/100$) is considered, and a commercial full-wave code [36], based on the infinite array approximation, is adopted.

The unit cell is optimized to satisfy condition (2) and thus maximize function (1) at the following operating frequencies, $f_1 = 878\text{MHz}$ and $f_2 = 956\text{MHz}$.

The design procedure of the proposed dual-band MA cell follows the rules outlined in [7] for the single frequency fractal MA cell. Each n-resonant element, with n $\in\{1, 2\}$, is characterized by an $L_n \times L_n$ square patch, which is properly reshaped by subtracting a smaller $S_nL_n \times S_nL_n$ square from the center of its edges (Fig. 6), where S_n is the scale factor varying from 0 to 1/3. As demonstrated in [54] and discussed in the previous subsection, the adopted fractal patch allows to accommodate a greater electrical length into a smaller cell (i.e. for $S_n \neq 0$, the resonant length of the fractal patch, equal to $(1+2S_n)L_n$ [7], is longer with respect to that of the beginning $L_n \times L_n$ square patch). Moreover, as can be clearly observed in [54], the miniaturization capability of the proposed fractal element becomes more relevant when a higher value of S is considered and/or the fractal order increases. For the above reasons, a proper reduction of the patch length, L_n, is essential to shift up the resonance to the assigned operating frequency.

The synthesis procedure of the proposed MA cell consists in finding the optimal L_n and S_n values able to simultaneously meet the following goals: $f_{res} = \{f_1, f_2\}$, $Re\{Z_{cell}(f_{res})\} = 377\ \Omega$. To this end, as demonstrated in Fig. 7, it is useful to remember that the use of smaller patch lengths L_n gives higher resonance frequencies and vice versa [7], [29]. Conversely, the use of greater S_n-values allows to move down the resonance frequencies (refer to Fig. 8), also reducing the unit cell input impedance [7]. Then, a proper sizing of fractal patch parameters (i.e. L_n and S_n, $n = 1, 2$) allows to synthesize two distinct absorption peaks, one for each pair of resonators. Further details concerning the adopted synthesis process can be found in [7], where a graphical synthesis procedure is carefully described.

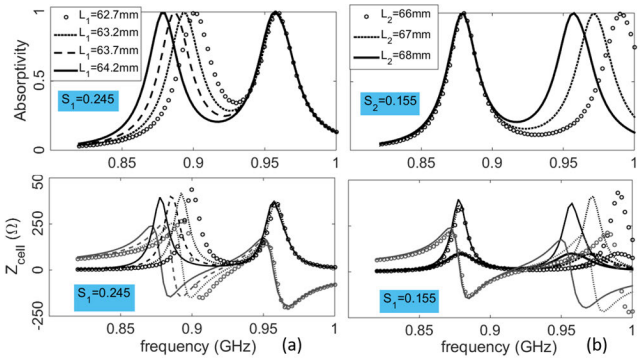

FIGURE 7. Parametric analysis of a dual-band fractal MA: (a) absorptivity and cell impedance for different patch length L_1 and fixed values of $S_1 = 0.245$, $L_2 = 68\text{mm}$, $S_2 = 0.155$; (b) absorptivity and cell impedance for different patch length L_2 and fixed values of $S_2 = 0.155$, $L_1 = 64.2\text{mm}$, $S_1 = 0.245$.

Fig. 9(b) shows the calculated absorption coefficient of the cell achieved at the end of the optimization process. Two absorption peaks greater than 99.5% are achieved at

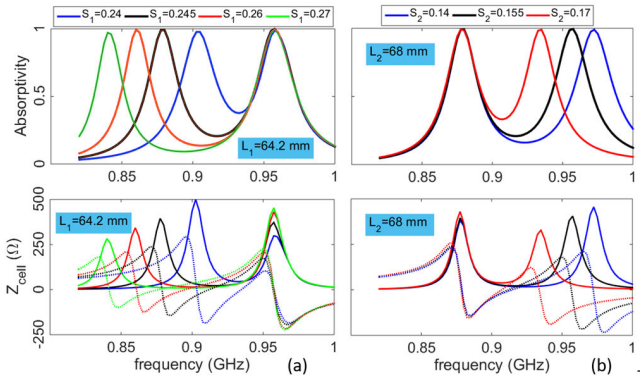

FIGURE 8. Parametric analysis of a dual-band fractal MA: (a) absorptivity and cell impedance for different scaling factor S_1 and fixed values of $L_1 = 64.2$mm, $L_2 = 68$mm, $S_2 = 0.155$; (b) absorptivity and cell impedance for different scaling factor S_2 and fixed values of $L_2 = 68$mm, $L_1 = 64.2$mm, $S_1 = 0.245$.

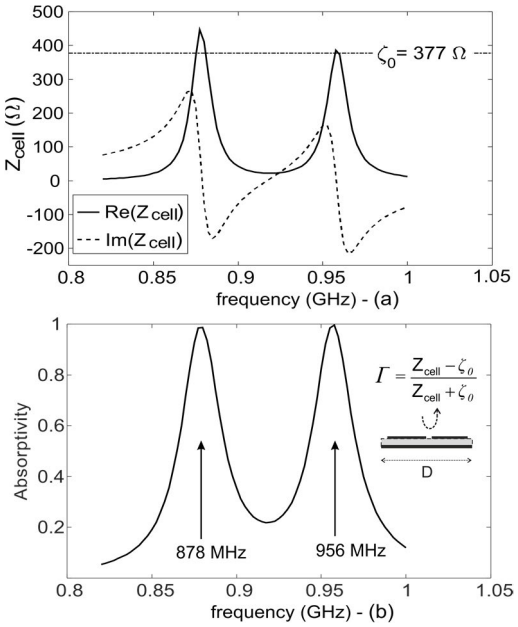

FIGURE 9. Synthesis of a dual-band fractal absorber sensor: (a) input impedance of the cell vs frequency; (b) absorptivity vs frequency.

the following UHF-frequencies: $f_1 = 878$ MHz and $f_2 = 956$MHz. The full width at half maximum (FWHM) bandwidth around the absorption peaks is equal to 2.8%, at the first resonance and 3.2% at the second resonance. It can be observed in Fig. 9(a) that the above peaks correspond to a well-matched cell impedance. The sizes of each fractal patch are depicted in Table 1.

TABLE 1. Dual-band MA cell dimensions.

Absorption peaks	f_1= 878 [MHz]		f_2= 956 [MHz]	
Patch dimensions	L_1 [mm]	S_1	L_2 [mm]	S_2
	64.2	0.245	68	0.155

Furthermore, a wide angular stability is obtained for both Transverse Electric (TE) and Transverse Magnetic (TM) polarizations (see Fig. 10). As a matter of the fact, the simulated unit cell absorptivity is insensitive to incident angle variations, showing very high and frequency-stable absorption peaks, for both considered polarizations. In Fig. 10, the absorption coefficient is computed by taking into account that the TE free space impedance increases as the incident angle increases (i.e. $\xi_0^{\mathrm{TE}} = \xi_0/\cos\theta$, where $\xi_0 = \sqrt{\mu_0/\varepsilon_0} = 377\Omega$) while the opposite is valid for TM polarization(i.e. $\xi_0^{\mathrm{TM}} = \xi_0 \cos\theta$).

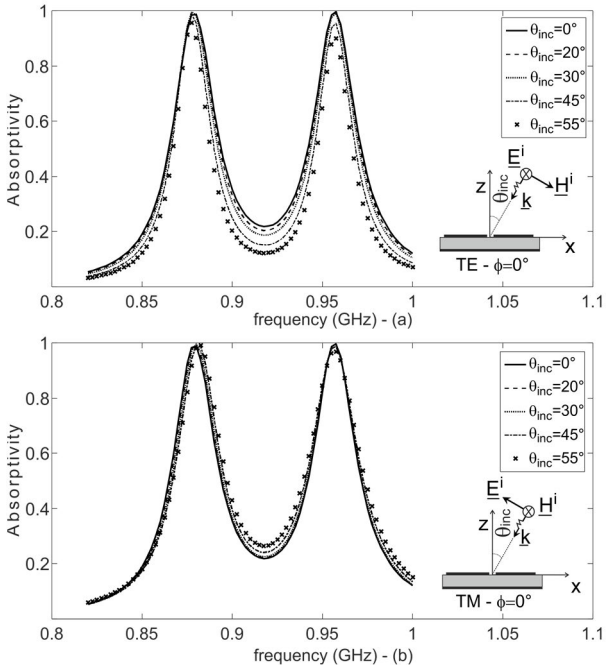

FIGURE 10. Absorptivity vs. frequency of the synthesized dual-band MA sensor for different incidence angles: (a) TE-polarization (b) TM-polarization.

An absorption rate ranging from 95.6% to 99.7% with a root mean squared error (*rmse*) of approximately 2.85% with respect to the ideal 100% absorption value is achieved at f_1, and from 90% to 99.7% ($rmse = 5.64\%$) at f_2, for a TE polarized incident plane wave (Fig. 10(a)). Similarly, a peak value ranging from 98.8% up to 99.7% ($rmse = 0.91\%$) at f_1, and from 97% up to 99.7% ($rmse = 1.88\%$) at f_2 is obtained in the case of TM polarization (Fig. 10(b)). Finally, Fig. 11 shows that the proposed MA sensor is essentially insensitive to different polarization angles, in the presence of normal incidence.

The equivalent circuit model of the proposed MA unit cell is shown in Fig. 12. The unit cell impedance, Z_{cell}, is modelled as a parallel combination of the grounded substrate impedance, Z_h, and the FSS impedance, Z_{FSS}.

Z_h is calculated using the formula $Z_h = j\frac{\xi_0}{\sqrt{\varepsilon_r}}\tan\left(k\sqrt{\varepsilon}_r h\right)$, where $\frac{\xi_0}{\sqrt{\varepsilon_r}}$ is the characteristic impedance of the substrate. The metallic FSS is represented by two RLC-series circuits in parallel (Fig. 12), each given by $Z_{pn} = \mathrm{R}_n - \mathrm{j}\frac{1-\omega^2 \mathrm{L}_n \mathrm{C}_n}{\omega \mathrm{C}_n}$, with $n \in \{1, 2\}$, corresponding to the different patch pairs

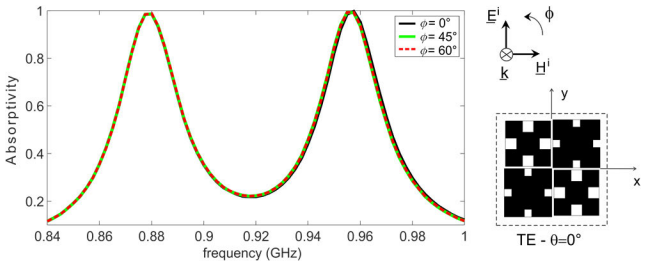

FIGURE 11. Absorptivity vs. frequency of the synthesized dual-band MA sensor for different polarization angles at normal incidence.

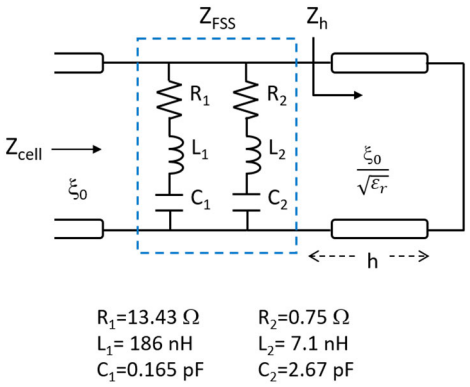

FIGURE 12. Equivalent circuit model of the proposed MA unit cell.

responsible for the MA resonances at f_1 and f_2, respectively (see Figs. 12 and 1(c)). The overall impedance of the metallic FSS is determined by the parallel combination of Z_{p1} and Z_{p2}, i.e. $Z_{FSS} = \frac{Z_{p1}Z_{p2}}{Z_{p1}+Z_{p2}}$. When the inductive impedance of the substrate Z_h and the imaginary part of Z_{FSS} are equal and opposite (i.e., $Im\{Z_{FSS}\} = -Z_h$), the unit cell resonates. As a result, the impedance Z_{cell} becomes purely real (for thin substrates [57]) and equal to the free space impedance ξ_0, resulting in two absorption peaks.

More specifically, the lumped elements in Fig.12 assume the following meaning: the resistors R_1 and R_2 take into account the ohmic/dielectric losses; L_1 and L_2 represent the inductances of the cell due to the magnetic flux between the patches and the ground plane; finally, C_1 and C_2 denote the parasitic capacitance between the edges of adjacent patches and the capacitance between the patches and the ground plane due to the evanescent Floquet modes, in the case of thin substrates (h< 0.3D) [57], [52].

The lumped parameters mentioned above can be numerically retrieved through a full-wave simulation of the unit cell reflection coefficient Γ, following the approach described in [7], [56], and [57]. The impedance Z_{FSS} can be calculated using the formula provided by the equivalent circuit in Fig. 12:

$$Z_{FSS} = \frac{\xi_0 Z_h (1+\Gamma)}{(Z_h - \xi_0) - \Gamma (Z_h + \xi_0)} \tag{3}$$

The capacitance and inductance values can be determined by calculating the null of the imaginary part of the FSS impedance, i.e. the frequencies f_{pn} at which $Im\{Z_{FSS}\} = 0$. At such resonances, the capacitances C_n are related to the inductances L_n by the well-known relationship given by $C_n = 1/(2\pi f_{pn} L_n)$ [58]. Once this condition is imposed, the inductances can be obtained by solving an equation system that enforces the resonance condition of the MA cell at the operating frequencies f_1 and f_2 (i.e. $Im\{Z_{FSS}\} = -Z_h$ [57]). The values of the resistors R_1 and R_2 can then be estimated from the real part of expression (3).

The calculated values of the equivalent circuit components are shown in Fig. 12. Finally, a good agreement between the full-wave simulations and the circuit model results can be observed in Fig. 13, confirming the validity of the adopted model.

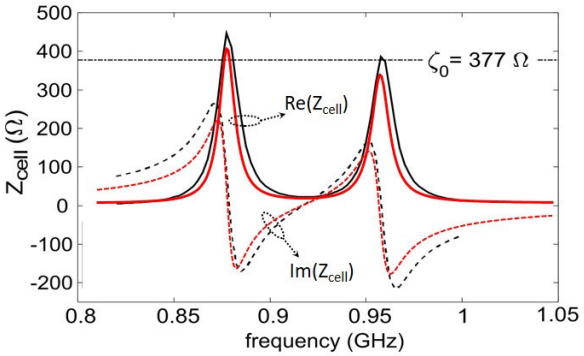

FIGURE 13. Full-wave simulations (black line) and circuit model results (red line).

In order to explain the fundamental physics behind the absorption mechanism of the proposed dual-band MA cell, the electric field distribution (Fig. 14) and the surface current (Fig. 15) are computed under normal incidence, in correspondence of the two absorption frequencies.

Both figures clearly illustrate that the different pairs of fractal patches, labelled as #1 and #2 (Fig. 14), are respectively responsible for the absorption at the resonating frequencies f_1 and f_2. In particular, the induced electric field due to the incident EM wave is strongly concentrated on the surface of the corresponding resonating pair of patches, namely on patches #1, for $f_1 = 878$MHz (Fig. 14(a)), and on patches #2, for $f_2 = 956$MHz (Fig. 14(b)).

Contextually, the incident magnetic field generates antiparallel current between each pair of patches and the ground plane (see Figs. 15(a) and 15(b)), at the corresponding resonating frequency. These out-of-phase currents develop a circulating current loop that is perpendicular to the magnetic field of the incident wave. The above electric and magnetic responses overlap each other at resonant frequencies, thus realizing a strong EM wave absorption.

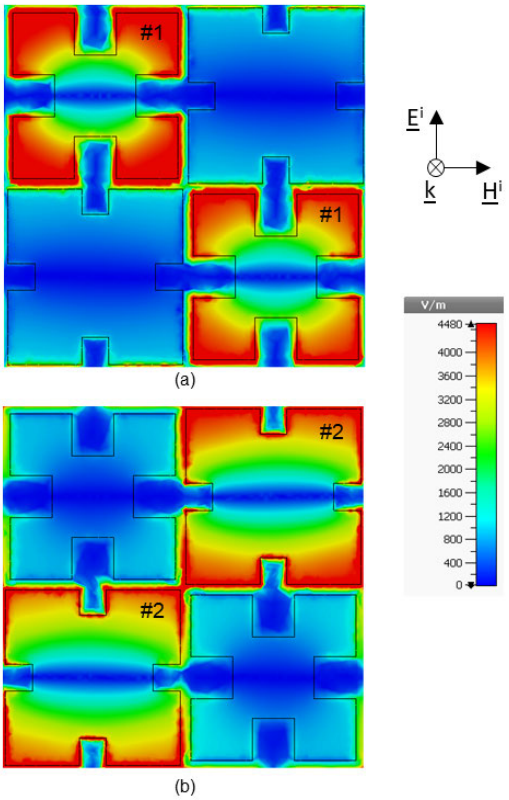

FIGURE 14. E-field distribution at (a) 878 MHz, and (b) 956 MHz.

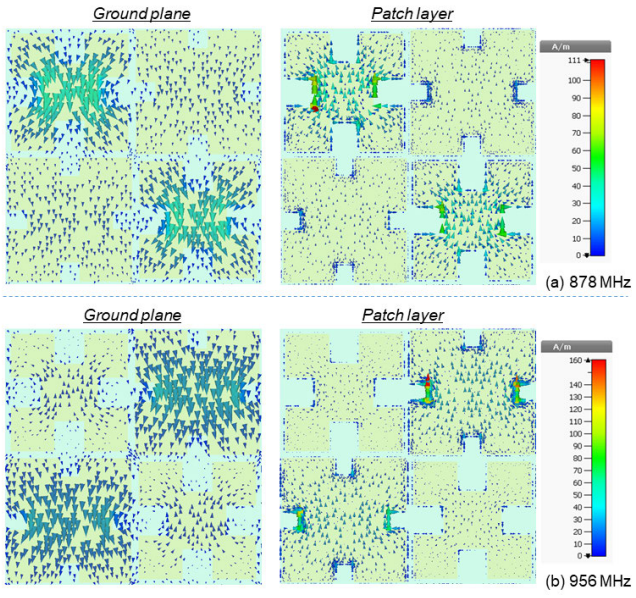

FIGURE 15. Surface current distribution at (a) 878 MHz, and (b) 956 MHz.

C. FRACTAL UNIT CELL POTENTIALITIES AND APPLICATIONS

As demonstrated in the following, the proposed fractal-based MA cell is very versatile, being able to offer the capability of multiple distinct absorption peaks or broadband absorption features. A proper tuning of fractal dimensions allows to easily move the separation distance between the MA absorption peaks [59], depending on the applications requirements.

As illustrated in Fig. 16, for example, a bandwidth-enhanced MA cell can be achieved by properly re-sizing the double resonant cell designed in the previous section.

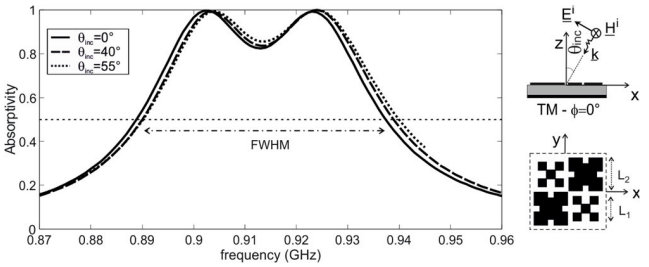

FIGURE 16. Absorptivity vs. frequency of a broad-band fractal absorber sensor for different incidence angles (TM-polarization).

In this case, both the substrate features as well as the inter-element spacing D (Fig. 1) are left unchanged, while the patches sizes are modified to the following values: $L_1 = 69.1$ mm – $S_1 = 0.17$, $L_2 = 52$ mm – $S_2 = 0.31$, (see Figs. 1 and 16). This leads a FWHM of 6% at 915 MHz (about two times greater than those achieved for the dual-band cell of Fig. 9). Furthermore, as shown in Fig. 16, excellent angular stability is also obtained in this case.

The versatility of the proposed multi-band configuration is finally confirmed through the design of a tri-band MA sensor operating within the GSM frequencies [29].

The layout depicted in Fig. 17 is considered, consisting of three different groups of identical miniaturized Minkowski elements. The unit cell size is fixed to a value of 0.4λ at the lower resonant frequency, while the substrate features are fixed to the following values: $\varepsilon_r = 4.4$, $\tan\delta = 0.02$, h = 3.2mm $\leq \lambda_0/100$. Even in this case, a fine adjustment of the fractal patches sizes (i.e. L_n and S_n, n = 1, 2, 3 - see Fig. 17), leads to the desired multi-band operation mode.

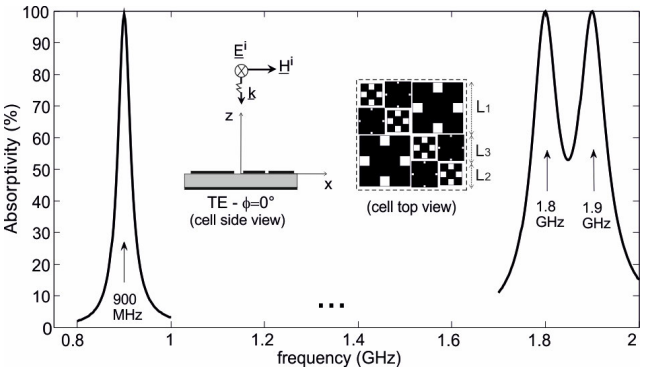

FIGURE 17. Absorptivity vs. frequency of a three-band fractal absorber sensor for different incidence angles (TM-polarization).

Three absorption bands are achieved in a neighborhood of the frequency values $f_1 = 0.9$ GHz, $f_2 = 1.8$ GHz, $f_3 = 1.9$ GHz, by fixing the following patches sizes (Fig.17):

$L_1 = 66.3$mm - $S_1 = 0.192$, $L_2 = 27.3$mm - $S_2 = 0.29$, $L_3 = 33.85$mm - $S_3 = 0.1$.

The proposed triple-band MA cell, giving very high absorption rates greater than 99% and quite good angular stability, is suitable for EMI detection/reduction within the GSM band.

D. FREQUENCY SCALABILITY OF THE FRACTAL-BASED UNIT CELL

As further proof of the versatility of the proposed fractal MA configuration, the unit cell is re-scaled to work at different frequency bands. In particular, the cell is designed to operate within S and C bands, by properly tuning unit cell sizes, comprising inter-element spacing D, substrate thickness, and patches sizes. All the above geometric parameters are proportionally resized with respect to the relative operating wavelengths, by using the same FR-4 material ($\varepsilon_r = 4.2$) as dielectric substrate. The designed unit cell has the following sizes: $D = 32$mm, $h = 0.762$mm, $L_1 = 15$ mm $- S_1 = 0.245$, $L_2 = 14.5$ mm $- S_2 = 0.155$, (see Fig. 1). As shown in Fig. 18, two absorption peaks of about 99.8% and 99.5% are respectively achieved at the following frequencies: $f_1 = 3.72$ GHz and $f_2 = 4.5$GHz. The FWHM is equal to 3%, at the first resonance and 3.1% at the second resonance. In conclusion, even the scaled dual-band MA cell offers very high absorption rates, and good frequency selectivity, making it suitable for sensing and/or EMI reduction applications within S and C bands.

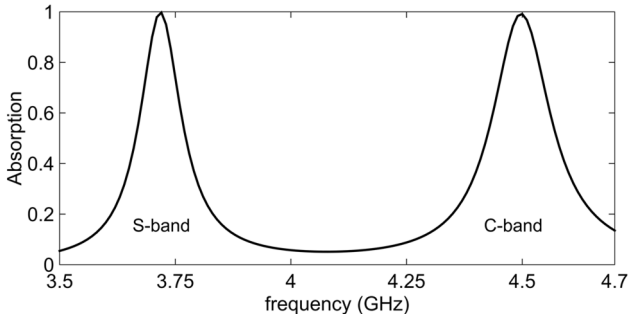

FIGURE 18. Absorptivity vs. frequency of a dual-band absorber sensor for S and C bands (TM-polarization).

The only limitation of the proposed fractal geometry is related to the manufacturing precision of the numerically controlled mechanical milling techniques, which becomes relevant only at very high frequencies, namely above 40 GHz. The same authors have in fact successfully designed and realized a Ka-band fractal-based reflectarray for mmWaves applications [60]. When considering higher frequencies, photolithographic manufacturing techniques are required. The aforementioned high versatility of the proposed fractal configuration allows to design ad-hoc MA devices for different applications, ranging from SAR and EMI reduction [7], to energy harvesting [61] and sensing. As just demonstrated, the proposed MA cell allows to have a single MA structure offering broadband, multi-band and/or high selectivity behavior.

III. SENSING APPLICATIONS

The absorption features of metamaterial absorbers depend on the impedance matching between MA cell and free space at given resonant frequencies (see Section II). As it is well known, the above condition is strictly related to the properties of the substrate layers composing the cell. Hence, absorption percentage and relative frequency position can be handled by varying substrate dielectric constant and thickness. Exploiting the above concept, MAs can be adopted for material diagnostics applications, by interposing a sensing layer, namely the sample under test (SUT), between the printed metallic pattern and the ground plane or, in alternative, by placing the sensing layer on the top of MA patches. The latter approach is considered in this paper to investigate the sensing capabilities of the proposed MA. The SUT is placed on the top of MA structure, as a covering layer of the metallic fractal patches (see Fig. 19). The sensing of material characteristics is performed by detecting the frequency shift in MA absorption peaks due to the change in the SUT dielectric constant values.

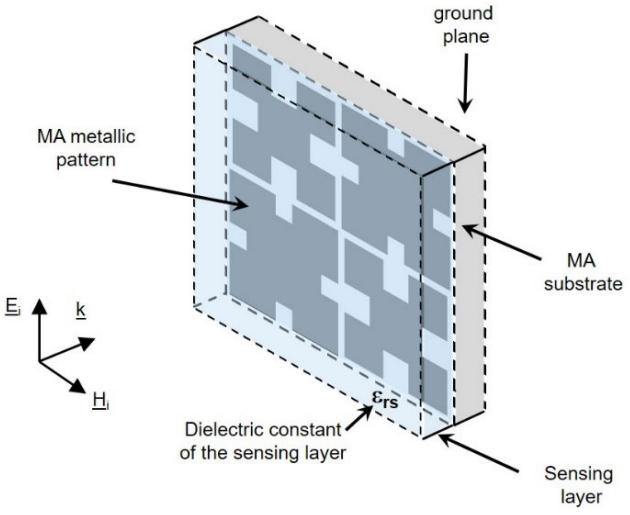

FIGURE 19. MA-based sensor model.

In particular, the designed dual-band MA (see section II-B) is proposed as a MA-based sensor, due to its higher frequency selectivity (namely its smaller FWHM), which is a valuable feature for detecting and discriminating any variations that occur in the sensing layer. Indeed, a narrower peak may provide a better resolution for the frequency shift caused by the variation of SUT dielectric constant.

Different substrate materials with dielectric constants ranging from 2.17 to 3.6 and a fixed thickness of 3.2 mm are tested. As shown in Fig. 20, the integration of the sensing layer with the designed MA cell causes a shift of the absorption peaks in both frequency bands with respect to the absorption diagram of the unloaded MA (Fig. 9(b)).

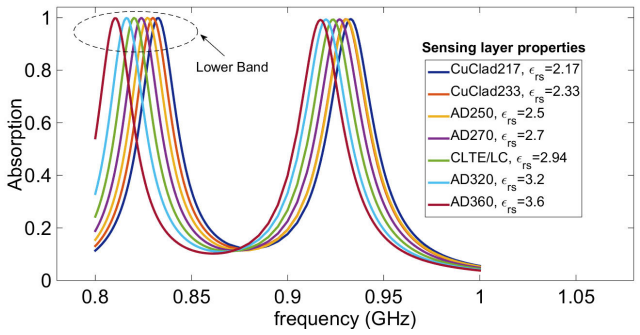

FIGURE 20. Absorption of the MA-based sensor for different SUTs.

This feature allows the proposed configuration to be successfully used for the dielectric characterization of low loss materials at two frequencies in a single step.

In particular, at the first resonance the absorption peak moves from 878 MHz (unloaded MA – Fig. 9) down to 833 MHz, for a sensing layer consisting of a sheet of Arlon CuClad 217 ($\varepsilon_{\rm rs} = 2.17$). At the same time, the 2nd resonance peak shifts from 956 MHz (unloaded MA - $\varepsilon_{\rm rs} = 1$) down to 933 MHz for a SUT with a dielectric constant equal to $\varepsilon_{\rm rs} = 2.17$. Afterward, by progressively increasing the dielectric constant of the sensing layer, both resonance peaks gradually move towards smaller frequencies (1st resonance $\rightarrow$ 810 MHz, 2nd resonance $\rightarrow$ 917 MHz for a SUT composed by Arlon AD360 layer - $\varepsilon_{\rm rs} = 3.6$), maintaining an amplitude always close to unity (Fig. 20).

The overall variation of the absorption peaks frequency position vs the SUT dielectric constant is reported in Fig. 21, both at the lower (Fig. 21(a)) and the upper band (Fig. 21(b)). The dashed line shows the linear fitting for the retrieved data.

The fitting function in Fig. 21(a) is described by $f = -15.85\varepsilon_{rs} + 866.81$, where the dependent variable f is the resonance frequency and the independent variable ε_{rs} represents the relative dielectric constant of the SUT, while the fitting function in Fig. 21(b) is described by $f = -11.59\varepsilon_{rs} + 958.13$. It can be observed from Fig. 21 that the simulated data (i.e. blue diamond markers in Fig. 21(a) and blue cross markers in Fig. 21(b)) roughly match the linear functions with quite small errors in the fitting parameters, equal to about $\pm 0.4MHz$ for the lower band and $\pm 0.8MHz$ for the upper band.

The extracted sensitivities $S(\%)$ of the MA sensor is computed for both frequency bands as follows [42], [62]:

$$S\,(\%) = \frac{(f - f_0)}{f_0(\varepsilon_{rs} - 1)} \times 100 \qquad (4)$$

where f is the initial frequency (when the MA is unloaded), f_0 is the frequency when the sample under test is placed on the top of MA and $\varepsilon_{\rm rs}$ is the permittivity value of the material under test. The sensitivity of the proposed MA sensor is equal to about 4.6 and 2.1 in correspondence of the 1st and the 2nd resonance, respectively. As a further quantitative description of the sensing performance, the Figure of Merit (FoM) of the

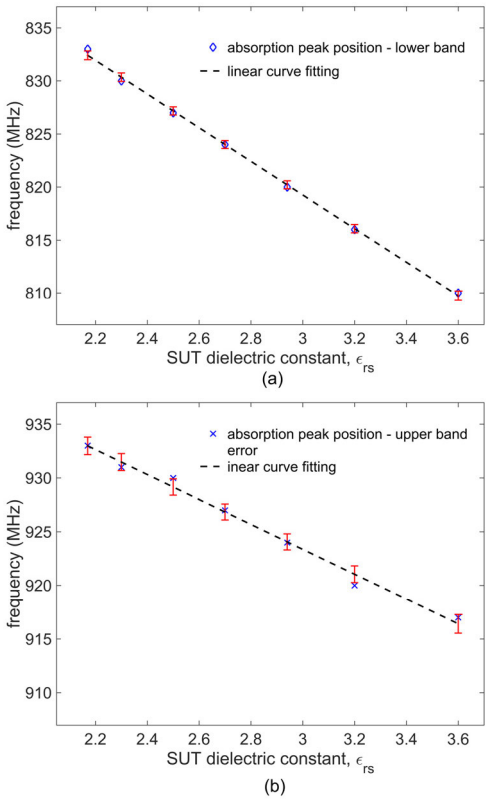

FIGURE 21. Absorption peak position vs dielectric constant values of SUTs: (a) 1st resonance; (b) 2nd resonance.

proposed MA-based sensor is calculated as FoM = S×Q, where S is the sensitivity (see (4)) and Q is the resonator quality-factor given by $Q = f_r/\Delta f$, with f_r and Δf the resonance frequency and the 3dB bandwidth, respectively. The proposed sensor FoM is equal to about 160 at the lower band and 74 at the upper band. In conclusion, the sensor works quite well at both frequency bands, but it shows higher performance and better resolutions at the lower resonance.

A detailed comparison of the proposed MA sensor with recent relevant works, based on the use of MA absorbers, is reported in Table 2, considering unit cell size, thickness, substrate, operation frequency bands, absorption peaks percentage, polarization insensitive behavior.

Both dual-band cell designs, respectively discussed in subsections II-A (Design #1 - UHF band cell) and II-C (Design #2 – S/C band cell), are reported in the table.

As it can be observed, the proposed MA unit cells are thinner and smaller in size than previous MA-based configurations. Similarly to other existing configurations, they allow to reach very high absorption peaks ($\geq$ 99.5%) and a polarization insensitivity behavior. In contrast to other configurations in the literature [11], [14], [40], [41], [28], the absorption peaks of the proposed MA sensor always maintain an amplitude close to unity for different values of the SUT (see Fig. 20). This guarantees excellent detection performance [14]. Finally, Table 3 depicts a comparison of various frequency variation sensors, where f is the resonating

TABLE 2. Comparison of proposed MA-based sensor with recent works.

Ref.	Unit cell volume	Substrate	Operating frequencies (GHz)	Absorption peaks (%)	Polarization insensitive	Function
[11]	0.75λ×0.75λ ×0.035λ	DiClad 527 ε_r=2.5	6.46 7.68	Not specified	Not Specified	Absorber
[12]	0.92λ×0.92λ ×0.073λ	FR-4 ε_r=4.6	13.78 15.3	99.6 99.6	Yes	Absorber
[14]	0.42λ×0.42λ ×0.067λ	FR-4 ε_r=4.3	12.62 14.12 17.53 19.91	97 99.51 99 99.5	Yes	Absorber
[16]	0.36λ×0.36λ ×0.078λ	Polymide ε_r=3.5	750- 1730	90	Yes	Absorber / Polarization Converter
[39]	0.33λ×0.69λ ×0.049λ	FR-4 -Rogers RO4350B	9.06 11.16	96.8 88.4	Not Specified	Absorber
[40]	0.44λ×0.44λ ×0.088λ	FR-4 ε_r=4.3	14.62 16.30	99.9 99.9	Yes	Absorber
[41]	0.72λ×0.72λ ×0.115λ	FR-4 ε_r=4.3	21.6 24.04	99.9 99.9	Yes	Absorber
[42]	0.72λ×0.32λ ×0.0473λ	FR-4 ε_r=4.3	9.46	99.6	Not Specified	Absorber
[43]	0.35λ×0.35λ ×0.0525λ	FR-4 ε_r=4.3	105	99.7	Not Specified	Absorber
[48]	0.33λ×0.33λ ×0.013λ	ε_r=4.4	4.13	90	Not Specified	Absorber
[28]	0.9λ×0.9λ ×0.068λ	ZnSe	33930 36270 38390	98.5 99.3 99.6	Not Specified	Absorber
Design 1	0.4λ×0.4λ ×0.0094λ	FR-4 ε_r=4.2	0.878 0.954	99.7 99.7	Yes	Absorber
Design 2			3.72 4.5	99.8 99.5	Yes	

TABLE 3. Sensitivity comparison of various frequency-variation sensors.

Ref.	f(GHz)	S (%)	Q	*MA-based*	*Near-unity peak*
[45]	0.87	0.91	-	no	-
[46]	4.16	1.18	43	no	-
[47]	3.75	1.019	-	no	-
[63]	2.64	4.4	28	no	-
[14]	12.62 14.12 17.53 19.91	- - - 4.6	- - - 34.32	yes	yes (only 4th absorption peak)
[39]	9.06 11.16	1.29 1.13	387 325	yes	-
[40]	14.62 16.30	- 5.3	34.8 33.95	yes	yes (only 2nd absorption peak)
[42]	9.46	0.56	135	yes	-
[43]	105	4.6	19.6	yes	yes
[48]	4.13	2.1	78	yes	no
[28]	33930 36270 38390	2.13 1.82 2.22	Not Specified	yes	yes (only 1st and 3rd absorption peaks)
Present work	***Design 1*** 0.878 0.956 ***Design 2*** 3.72 4.5	 4.6 2.1 4.6 3.33	 36 33 33.3 32.3	yes	yes

frequency of unloaded sensors and $S(\%)$ is the average relative sensitivity computed by the formula (4). Most of the works cited in the table are described in [49], which gives a comprehensive outlook on various methodologies to enhance the performance of planar microwave sensors, such as sensitivity, resolution and robustness (for example using machine learning [50]). According to the results in Table 3, the proposed MA sensor has the highest average relative sensitivity. Additionally, the analysis of both tables indicates that the proposed configuration provides a good balance between sensitivity, quality factor (Q), and unit cell size when compared to other MA-based sensors.

Concerning future developments, the sensor ability of the proposed MA to detect the change in materials dielectric constant will be extended to other useful sensing applications, at different frequency bands. In particular, by exploiting the relationships, already known and tabulated in the literature, between the dielectric constant of specific materials with other physical and/or environmental parameters [11], [14], [64], [65], such as density and humidity, it will be possible to develop MA-based multifunctional sensors.

IV. EXPERIMENTAL RESULTS

In order to validate the proposed dual-band MA configuration, a 126cm×126cm absorber panel, composed by 9×9 0.4λ-cells, is realized and tested in the microwave anechoic chamber of the University of Calabria. A far-field measurement setup (Fig. 22), consisting of a pair of transmitting/receiving broadband horn antennas [66], is adopted to detect the reflection response of the absorbing panel and then to retrieve its absorptivity features vs. frequency, for different polarizations of the incident field. Both horn antennas are connected to a 2-port Anritsu 37217C Vector Network Analyzer (VNA) using low-loss flexible cables. The antennas are positioned in front of the sample at a distance of 180 cm, satisfying the far-field condition (i.e. $d>2D^2/\lambda$, where d is the distance between the sample and the pairs of antennas, λ is the wavelength of the incidence EM signal, and D is the diagonal length of the horn antennas). As illustrated in Figs. 22(a) and 22(b), the horns are coherently rotated on their own axis in order to perform the measurements, for both the TE as well as the TM polarization. The reflection measurements are calibrated using a planar sheet of aluminum as a reflecting mirror (Fig. 22), having the same sizes and position of the absorbing panel under test. Initially, the reflection coefficient of the aluminum sheet is measured as a reference. Afterwards, the reflection coefficient of the MA prototype is acquired and processed as follows, in order to retrieve the absorptivity coefficient $A_{MA}(f)$:

$$A_{MA}(f) = \frac{|\Gamma_{Al}(f)|^2 - |\Gamma_{MA}(f)|^2}{|\Gamma_{Al}(f)|^2} \tag{5}$$

where $\Gamma_{Al}(f)$ and $\Gamma_{MA}(f)$ are the measured reflection coefficients (i.e. the S_{21}-parameter of the adopted 2-port measurement setup illustrated in Fig. 22) of the aluminum-sheet and the MA panel, respectively. The above formula allows to normalize the MA response with respect to the adopted reference metal sheet, also removing the influence of environmental noise, such as unwanted edge scattering.

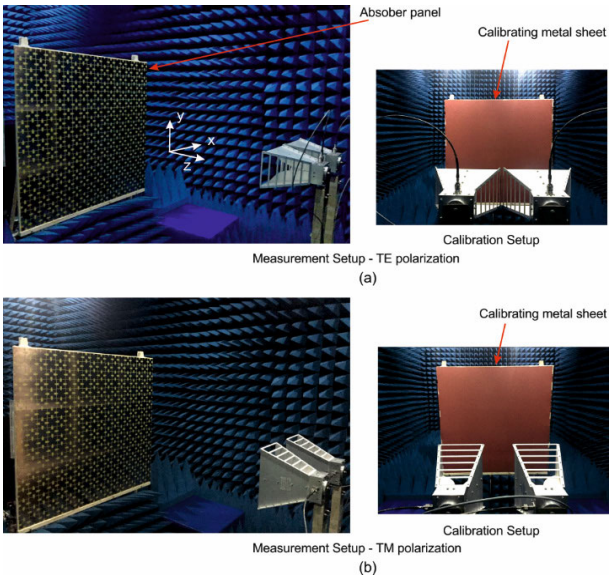

FIGURE 22. Free-space measurement setup: (a) TE polarization; TM-polarization.

As a first validation, the absorptivity of the MA panel is measured under normal incidence (i.e. $\theta_{inc} = 0$ – see Fig. 22), for both TE and TM polarizations. A very good agreement can be observed between measured and simulated data (Fig. 23), with a very little and negligible frequency shift (< 2MHz) in the position of the absorption peaks.

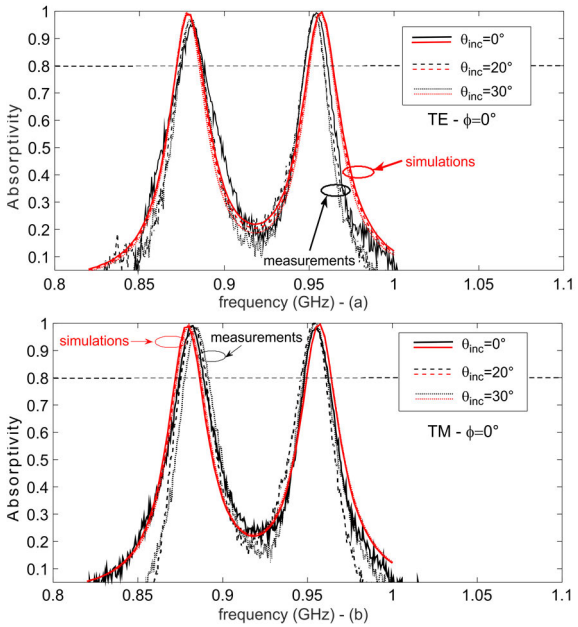

FIGURE 23. Comparison between measured and simulated absorptivity vs. frequency for different incidence angles: (a) TE-polarization; TM-polarization.

Finally, in order to measure the absorptivity of the MA panel for different oblique incident angles, the angular position of the transmitting horn antenna (i.e. θ_{inc} in Fig. 24) is moved from 0° up to 30° on the xz-plane and, coherently, the receiving horn is moved in the specular directions, satisfying the Snell's law (Fig. 24). Even in these latter cases, a good agreement can be observed in Fig. 23 between measured and simulated data, showing that the proposed fractal MA panel is able to offer perfect absorption features and a quite good angular stability.

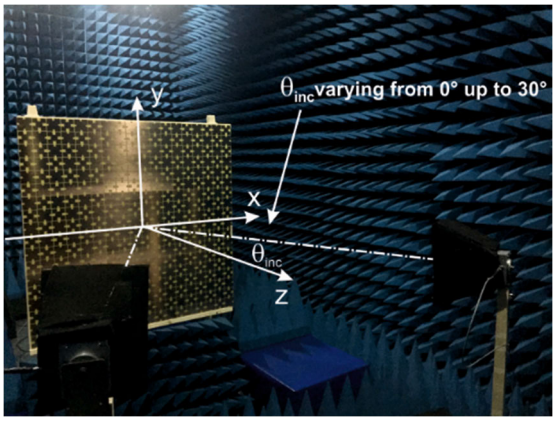

FIGURE 24. Free-space measurement setup under different incident angles.

As a final point, the sensing capabilities of the proposed metamaterial absorber are preliminary tested by considering one of the 3 × 3-cell subpanels (Fig. 25) composing the absorber panel illustrated in Figs. 22 and 24. A monostatic measurement setup is adopted to detect the reflection response of the MA sample and thus recover its absorption characteristics as a function of frequency, under normal incidence condition (see Fig. 25). An open boundary quad-ridged horn [67], connected to a VNA, is positioned at a distance of 1 m from the MA panel to satisfy the far-field condition. Measurements are taken outside the anechoic chamber to test the sensing capabilities of the proposed MA in uncontrolled environmental noise level conditions. The measurements are recorded at a temperature of 23°C and a relative humidity (RH) of 45%RH. The absorptivity measurement is calibrated using a metallic plate identical in size to the MA sample (see equation (5)). Fig. 25(a) illustrates the comparison between the simulated and measured absorptivity of the unloaded MA sensor, showing very good agreement at both absorption peaks. Small discrepancies are observed in the frequency range outside the absorption peaks, mainly due to scattering phenomena at the edges of the smaller MA sub-panel and to spurious reflections occurring in the measurement setup. To mitigate these effects, a time-domain gating (TDG) technique is applied by using the VNA [68] to measure only the signal reflected from the prototype sample. Finally, two different wood samples are tested (see the SUTs in Fig. 25(b)), having a dielectric constant equal to $\varepsilon_r = 1.76$ [69], [70] and a thicknesses of 3.2 mm (red line) and 10 mm (blue line), respectively. As depicted in Fig. 25(b), the measured results confirm the ability of the proposed MA

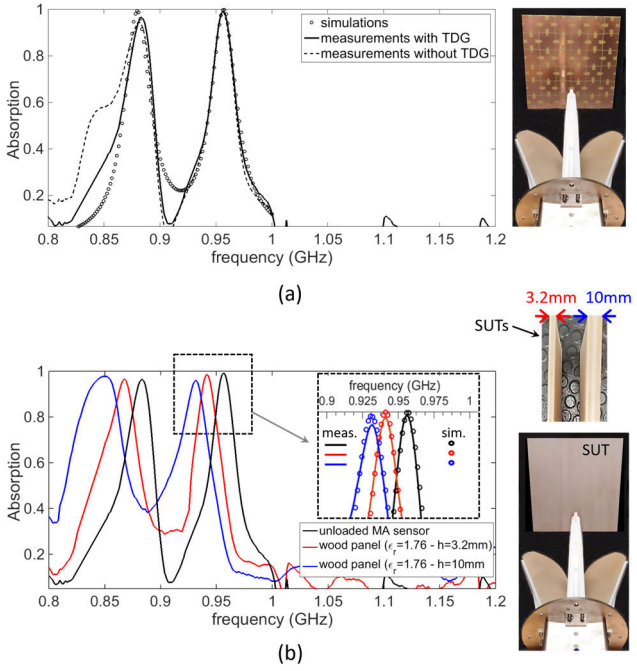

FIGURE 25. Experimental results: (a) comparison between simulated and measured absorptivity of the unloaded MA sensor; (b) measured absorptivity of the MA-based sensor for different SUTs.

to detect variations in the dielectric properties and thickness of the material under test.

V. CONCLUSION

Multi-frequencies fractal MA sensors have been proposed for ultra-low-frequency applications. The miniaturization skills of the adopted fractal shape have been exploited to implement a multi-band and ultra-thin absorber, operating within the UHF frequency range. Two pairs of miniaturized fractal metallic resonators have been accommodated within the same sub-wavelength MA-cell, thus achieving dual-band perfect absorption. Full-wave simulations and an equivalent circuit model have numerically demonstrated absorption rates of over 99% and good angular stability, confirming the validity of the proposed model. The sensing ability of the proposed MA has been proved, by effectively detecting the shift in its absorption peaks due to the change in the dielectric constant values of the sample under test. Good sensing performances in terms of sensitivity and figure of merit (FoM) have been demonstrated. In order to prove the validity of the proposed MA configuration, a dual-band MA panel has been designed, fabricated and experimentally tested. Very high absorption rates (>99%), for wide incidence angles, have been detected in correspondence of the desired working frequencies (i.e. 878 MHz and 956 MHz), showing the effectiveness of the proposed design concept in realizing multi-band MA sensors. In future developments, the concept of fractals will be further exploited to enhance the miniaturization level of MA-based sensors. Additionally, the proposed MA absorber will be integrated with reconfigurable materials or components, such as PIN diodes, to implement switchable functions like absorption/polarization conversion [16], which can increase sensing capabilities, even exploiting a random distribution of elements, such as that adopted in the various design schemes for statistical arrays [71], [72], [73], [74], [75], [76], [77].

REFERENCES

[1] N. I. Landy, S. Sajuyigbe, J. J. Mock, D. R. Smith, and W. J. Padilla, "Perfect metamaterial absorber," *Phys. Rev. Lett.*, vol. 100, no. 20, 2008, Art. no. 207402.

[2] C. M. Watts, X. Liu, and W. J. Padilla, "Metamaterial electromagnetic wave absorbers," *Adv. Mater.*, vol. 24, no. 23, pp. 98–120, Jun. 2012, doi: 10.1002/adma.201200674.

[3] W. Zhu, "Electromagnetic metamaterial absorbers: From narrowband to broadband," in *Metamaterials and Metasurfaces*. London, U.K.: IntechOpen, 2018, doi: 10.5772/intechopen.78581.

[4] F. Costa, S. Genovesi, A. Monorchio, and G. Manara, "Low-cost metamaterial absorbers for sub-GHz wireless systems," *IEEE Antennas Wireless Propag. Lett.*, vol. 13, pp. 27–30, 2014.

[5] Y. Okano, S. Ogino, and K. Ishikawa, "Development of optically transparent ultrathin microwave absorber for ultrahigh-frequency RF identification system," *IEEE Trans. Microw. Theory Techn.*, vol. 60, no. 8, pp. 2456–2464, Aug. 2012.

[6] W. Zuo, Y. Yang, X. He, C. Mao, and T. Liu, "An ultrawideband miniaturized metamaterial absorber in the ultrahigh-frequency range," *IEEE Antennas Wireless Propag. Lett.*, vol. 16, pp. 928–931, 2017.

[7] F. Venneri, S. Costanzo, and G. Di Massa, "Fractal-shaped metamaterial absorbers for multireflections mitigation in the UHF band," *IEEE Antennas Wireless Propag. Lett.*, vol. 17, pp. 255–258, 2018.

[8] K. Chen, B. Zhu, N. Jia, B. Sima, J. Zhao, T. Jiang, and Y. Feng, "Ultrathin microwave absorber in wireless communication band made of Swiss roll metamaterial structure," in *Proc. IEEE Int. Wireless Symp. (IWS)*, Mar. 2014, pp. 1–4, doi: 10.1109/IEEE-IWS.2014.6864243.

[9] H.-T. Zhong, X.-X. Yang, C. Tan, and K. Yu, "Triple-band polarization-insensitive and wide-angle metamaterial array for electromagnetic energy harvesting," *Appl. Phys. Lett.*, vol. 109, no. 25, Dec. 2016, Art. no. 253904.

[10] K. P. Kaur, T. Upadhyaya, and M. Palandoken, "Dual-band compact metamaterial-inspired absorber with wide incidence angle and polarization insensitivity for GSM and ISM band applications," *Radioengineering*, vol. 27, no. 4, pp. 1025–1031, Sep. 2018.

[11] M. Bakir, M. Karaaslan, E. Unal, O. Akgol, and C. Sabah, "Microwave metamaterial absorber for sensing applications," *Opto-Electron. Rev.*, vol. 25, no. 4, pp. 318–325, Dec. 2017.

[12] A. Hoque, M. T. Islam, A. Almutairi, T. Alam, M. J. Singh, and N. Amin, "A polarization independent quasi-TEM metamaterial absorber for X and Ku band sensing applications," *Sensors*, vol. 18, no. 12, p. 4209, Nov. 2018.

[13] Y. Zhang, J. Zhao, J. Cao, and B. Mao, "Microwave metamaterial absorber for non-destructive sensing applications of grain," *Sensors*, vol. 18, no. 6, p. 1912, Jun. 2018.

[14] M. L. Hakim, T. Alam, M. T. Islam, M. H. Baharuddin, A. Alzamil, and M. S. Islam, "Quad-band polarization-insensitive square split-ring resonator (SSRR) with an inner Jerusalem cross metamaterial absorber for Ku- and K-band sensing applications," *Sensors*, vol. 22, no. 12, p. 4489, Jun. 2022.

[15] Y. Li, L. Zeng, H. Zhang, D. Zhang, K. Xia, and L. Zhang, "Multifunctional and tunable metastructure based on VO_2 for polarization conversion and absorption," *Opt. Exp.*, vol. 30, no. 19, pp. 34586–34600, 2022.

[16] S. Liao, J. Sui, and H. Zhang, "Switchable ultra-broadband absorption and polarization conversion metastructure controlled by light," *Opt. Exp.*, vol. 30, no. 19, pp. 34172–34187, 2022.

[17] Y. Ma and H. Zhang, "Wide-angle energy steering and magnetic information detection-coding of stacked ferrite-based elements in the gradient magnetic domain," *Opt. Laser Technol.*, vol. 156, Dec. 2022, Art. no. 108544.

[18] W. Jingxuan, R. Zhihao, and L. Chengkuo, "Metamaterial technologies for miniaturized infrared spectroscopy: Light sources, sensors, filters, detectors, and integration," *J. Appl. Phys.*, vol. 128, no. 24, Dec. 2020, Art. no. 240901, doi: 10.1063/5.0033056.

[19] H. Jiang, Z. Xue, W. Li, and W. Ren, "Multiband polarisation insensitive metamaterial absorber based on circular fractal structure," *IET Microw., Antennas Propag.*, vol. 10, no. 11, pp. 1141–1145, Aug. 2016.

[20] M. Amiri, F. Tofigh, N. Shariati, J. Lipman, and M. Abolhasan, "Miniature tri-wideband Sierpinski–Minkowski fractals metamaterial perfect absorber," *IET Microw., Antennas Propag.*, vol. 13, no. 7, pp. 991–996, Jun. 2019.

[21] N. Goyal and R. Panwar, "Minkowski inspired circular fractal metamaterial microwave absorber for multiband applications," *Appl. Phys. A, Solids Surf.*, vol. 129, no. 4, pp. 1–9, Apr. 2023.

[22] H.-X. Xu, G.-M. Wang, M.-Q. Qi, J.-G. Liang, J.-Q. Gong, and Z.-M. Xu, "Triple-band polarization-insensitive wide-angle ultra-miniature metamaterial transmission line absorber," *Phys. Rev. B, Condens. Matter*, vol. 86, no. 20, Nov. 2012, Art. no. 205104.

[23] F. Venneri, S. Costanzo, and A. Borgia, "Fractal metasurfaces and antennas: An overview for advanced applications in wireless communications," *Appl. Sci.*, vol. 14, no. 7, p. 2843, Mar. 2024, doi: 10.3390/app14072843.

[24] D. H. Wqrner and S. Ganguly, "An overview of fractal antenna engineering research," *IEEE Antennas Propag. Mag.*, vol. 45, no. 1, pp. 38–57, Feb. 2003, doi: 10.1109/MAP.2003.1189650.

[25] J. Angueraw, C. Borjaw, and C. Puente, "Microstrip fractal-shaped antennas: A review," in *Proc. 2nd Eur. Conf. Antennas Propag. (EuCAP)*, 2007, pp. 1–7, doi: 10.1049/ic.2007.1521.

[26] H. Ozpinar and S. Aksimsek, "Fractal interwoven resonator based penta-band metamaterial absorbers for THz sensing and imaging," *Sci. Rep.*, vol. 12, no. 1, p. 19758, Nov. 2022.

[27] M. A. Naveed, R. M. H. Bilal, M. A. Baqir, M. M. Bashir, M. M. Ali, and A. A. Rahim, "Ultrawideband fractal metamaterial absorber made of nickel operating in the UV to IR spectrum," *Opt. Exp.*, vol. 29, no. 26, pp. 42911–42923, Dec. 2021.

[28] A. G. Mazare, Y. I. Abdulkarim, A. S. Karim, M. Bakir, M. Taouzari, F. F. Muhammadsharif, B. Appasani, O. Altintas, M. Karaaslan, and N. Bizon, "Enhanced sensing capacity of terahertz triple-band metamaterials absorber based on Pythagorean fractal geometry," *Materials*, vol. 15, no. 18, p. 6364, Sep. 2022.

[29] F. Venneri, S. Costanzo, and A. Borgia, "A dual-band compact metamaterial absorber with fractal geometry," *Electronics*, vol. 8, no. 8, p. 879, Aug. 2019.

[30] J. W. Park, P. Van Tuong, J. Y. Rhee, K. W. Kim, W. H. Jang, E. H. Choi, L. Y. Chen, and Y. Lee, "Multi-band metamaterial absorber based on the arrangement of donut-type resonators," *Opt. Exp.*, vol. 21, no. 8, pp. 9691–9702, 2013.

[31] D. Singh and V. M. Srivastava, "Dual resonance shorted stub circular rings metamaterial absorber," *AEU-Int. J. Electron. Commun.*, vol. 83, pp. 58–66, Jan. 2018.

[32] M. Li, H.-L. Yang, X.-W. Hou, Y. Tian, and D.-Y. Hou, "Perfect metamaterial absorber with dual bands," *Prog. Electromagn. Res.*, vol. 108, pp. 37–49, 2010.

[33] X. Shen, T. J. Cui, J. Zhao, H. F. Ma, W. X. Jiang, and H. Li, "Polarization-independent wide-angle triple-band metamaterial absorber," *Opt. Exp.*, vol. 19, no. 10, pp. 9401–9407, 2011.

[34] F. Dincer, M. Karaaslan, E. Unal, K. Delihacioglu, and C. Sabah, "Design of polarization and incident angle insensitive dual-band metamaterial absorber based on isotropic resonator," *Prog. Electromagn. Res.*, vol. 144, pp. 123–132, 2014.

[35] N. Mishra, D. K. Choudhary, R. Chowdhury, K. Kumari, and R. K. Chaudhary, "An investigation on compact ultra-thin triple band polarization independent metamaterial absorber for microwave frequency applications," *IEEE Access*, vol. 5, pp. 4370–4376, 2017.

[36] L. Huang and H. Chen, "Multi-band and polarization insensitive metamaterial absorber," *Prog. Electromagn. Res.*, vol. 113, pp. 103–110, 2011.

[37] S. Ji, C. Jiang, J. Zhao, X. Zhang, and Q. He, "Design of a polarization-insensitive triple-band metamaterial absorber," *Opt. Commun.*, vol. 432, pp. 65–70, Feb. 2019.

[38] K. P. Kaur, T. K. Upadhyaya, and M. Palandoken, "Dual-band polarization-insensitive metamaterial inspired microwave absorber for LTE-band applications," *Prog. Electromagn. Res. C*, vol. 77, pp. 91–100, 2017.

[39] K. P. Kaur and T. Upadhyaya, "Wide-angle and polarisation-independent tri-band dual-layer microwave metamaterial absorber," *IET Microw., Antennas Propag.*, vol. 12, no. 8, pp. 1428–1434, Jul. 2018.

[40] M. L. Hakim, T. Alam, M. S. Soliman, N. M. Sahar, M. H. Baharuddin, S. H. A. Almalki, and M. T. Islam, "Polarization insensitive symmetrical structured double negative (DNG) metamaterial absorber for Ku-band sensing applications," *Sci. Rep.*, vol. 12, no. 1, p. 479, Jan. 2022.

[41] M. L. Hakim, T. Alam, A. F. Almutairi, M. F. Mansor, and M. T. Islam, "Polarization insensitivity characterization of dual-band perfect metamaterial absorber for K band sensing applications," *Sci. Rep.*, vol. 11, no. 1, p. 17829, Sep. 2021.

[42] M. R. Islam, M. T. Islam, M. S. Soliman, B. Bais, M. J. Singh, H. Alsaif, and M. S. Islam, "Metamaterial sensor based on reflected mirror rectangular split ring resonator for the application of microwave sensing," *Measurement*, vol. 198, Jul. 2022, Art. no. 111416.

[43] H. Singh, A. Gupta, R. S. Kaler, S. Singh, and A. S. Gill, "Designing and analysis of ultrathin metamaterial absorber for W band biomedical sensing application," *IEEE Sensors J.*, vol. 22, no. 11, pp. 10524–10531, Jun. 2022, doi: 10.1109/JSEN.2022.3168827.

[44] A. S. Saadeldin, M. F. O. Hameed, E. M. A. Elkaramany, and S. S. A. Obayya, "Highly sensitive terahertz metamaterial sensor," *IEEE Sensors J.*, vol. 19, no. 18, pp. 7993–7999, Sep. 2019, doi: 10.1109/JSEN.2019.2918214.

[45] P. Vélez, L. Su, K. Grenier, J. Mata-Contreras, D. Dubuc, and F. Martín, "Microwave microfluidic sensor based on a microstrip splitter/combiner configuration and split ring resonators (SRRs) for dielectric characterization of liquids," *IEEE Sensors J.*, vol. 17, no. 20, pp. 6589–6598, Oct. 2017.

[46] A. Salim and S. Lim, "Complementary split-ring resonator-loaded microfluidic ethanol chemical sensor," *Sensors*, vol. 16, no. 11, p. 1802, Oct. 2016.

[47] J. Muñoz-Enano, P. Vélez, M. Gil, and F. Martín, "Frequency-variation sensors for permittivity measurements based on dumbbell-shaped defect ground structures (DB-DGS): Analytical method and sensitivity analysis," *IEEE Sensors J.*, vol. 22, no. 10, pp. 9378–9386, May 2022.

[48] W. Zhang, J.-Y. Li, and J. Xie, "High sensitivity refractive index sensor based on metamaterial absorber," *Prog. Electromagn. Res. M*, vol. 71, pp. 107–115, 2018.

[49] N. Kazemi, M. Abdolrazzaghi, and P. Musilek, "Comparative analysis of machine learning techniques for temperature compensation in microwave sensors," *IEEE Trans. Microw. Theory Techn.*, vol. 69, no. 9, pp. 4223–4236, Sep. 2021.

[50] M. Abdolrazzaghi, V. Nayyeri, and F. Martin, "Techniques to improve the performance of planar microwave sensors: A review and recent developments," *Sensors*, vol. 22, no. 18, p. 6946, Sep. 2022.

[51] Y. Liang, M. Chen, L. Peng, and Z. Li, "A dual-function switchable and frequency tunable active frequency selective surface," *Int. J. RF Microw. Comput.-Aided Eng.*, vol. 31, no. 12, Dec. 2021.

[52] S. Costanzo and F. Venneri, "Miniaturized fractal reflectarray element using fixed-size patch," *IEEE Antennas Wireless Propag. Lett.*, vol. 13, pp. 1437–1440, 2014.

[53] A. K. W. Chee, "On the design principles of 3-D RESURF-enhanced RF SOI LDMOSFETs: Gate geometry optimization and rescaling," *IEEE Trans. Electron Devices*, vol. 69, no. 12, pp. 6523–6528, Dec. 2022.

[54] S. Costanzo, F. Venneri, G. Di Massa, A. Borgia, A. Costanzo, and A. Raffo, "Fractal reflectarray antennas: State of art and new opportunities," *Int. J. Antennas Propag.*, vol. 2016, pp. 1–17, Jan. 2016.

[55] *Ansoft Designer*. Accessed: Jan. 27, 2023. [Online]. Available: https://www.ansys.com

[56] F. Costa, S. Genovesi, A. Monorchio, and G. Manara, "A circuit-based model for the interpretation of perfect metamaterial absorbers," *IEEE Trans. Antennas Propag.*, vol. 61, no. 3, pp. 1201–1209, Mar. 2013.

[57] F. Costa, A. Monorchio, and G. Manara, "Analysis and design of ultra thin electromagnetic absorbers comprising resistively loaded high impedance surfaces," *IEEE Trans. Antennas Propag.*, vol. 58, no. 5, pp. 1551–1558, May 2010.

[58] F. Costa, A. Monorchio, and G. Manara, "An equivalent-circuit modeling of high impedance surfaces employing arbitrarily shaped FSS," in *Proc. Int. Conf. Electromagn. Adv. Appl.*, Turin, Italy, Sep. 2009, pp. 852–855.

[59] T. T. Nguyen and S. Lim, "Bandwidth-enhanced and wide-angle-of-incidence metamaterial absorber using a hybrid unit cell," *Sci. Rep.*, vol. 7, no. 1, p. 14814, Nov. 2017, doi: 10.1038/s41598-017-14792-0.

[60] S. Costanzo, F. Venneri, A. Borgia, and G. D. Massa, "Dual-band dual-linear polarization reflectarray for mmWaves/5G applications," *IEEE Access*, vol. 8, pp. 78183–78192, 2020.

[61] S. Costanzo and F. Venneri, "Polarization-insensitive fractal metamaterial surface for energy harvesting in IoT applications," *Electronics*, vol. 9, no. 6, p. 959, Jun. 2020, doi: 10.3390/electronics9060959.
[62] M. Abdolrazzaghi, M. Daneshmand, and A. K. Iyer, "Strongly enhanced sensitivity in planar microwave sensors based on metamaterial coupling," *IEEE Trans. Microw. Theory Techn.*, vol. 66, no. 4, pp. 1843–1855, Apr. 2018.
[63] L. Zeng, B.-X. Li, and H.-F. Zhang, "Nonreciprocal electromagnetically induced unidirectional absorption based on the quasi-periodic metastructure and its application for permittivity sensing," *IEEE Trans. Instrum. Meas.*, vol. 72, pp. 1–12, 2023.
[64] J. Sui, R. Dong, S. Liao, Z. Zhao, Y. Wang, and H. Zhang, "Janus metastructure based on magnetized plasma material with and logic gate and multiple physical quantity detection," *Annalen der Physik*, vol. 535, no. 3, Mar. 2023, Art. no. 200509.
[65] J. Virtanen, L. Ukkonen, T. Björninen, and L. Sydänheimo, "Printed humidity sensor for UHF RFID systems," in *Proc. IEEE Sensors Appl. Symp. (SAS)*, Limerick, Ireland, Feb. 2010, pp. 269–272, doi: 10.1109/SAS.2010.5439426.
[66] *A-INFO LB-880 0.8÷8GHz Broadband Horn Antenna*. Accessed: Jan. 27, 2023. [Online]. Available: www.ainfoinc.com/antenna-products
[67] *A-INFO Pen Boundary Quad-Ridged Dual Polarization Horn Antenna 0.4–6 GHz*. Accessed: Sep. 19, 2023. [Online]. Available: www.ainfoinc.com/antenna-products
[68] *Anritsu 37217C Vector Network Analyzer Operation Manual*, Anritsu Company, Morgan Hill, CA, USA, 2004.
[69] R. Cicchetti, V. Cicchetti, S. Costanzo, P. D'Atanasio, A. Fedeli, M. Pastorino, S. Pisa, E. Pittella, E. Piuzzi, C. Ponti, A. Randazzo, M. Santarsiero, G. Schettini, and O. Testa, "A microwave imaging system for the detection of targets hidden behind dielectric walls," in *Proc. 33rd Gen. Assem. Scientific Symp. Int. Union Radio Sci.*, Rome, Italy, Aug. 2020, pp. 1–4, doi: 10.23919/URSIGASS49373.2020.9232008.
[70] S. Costanzo, G. Di Massa, M. Pastorino, and A. Randazzo, "Hybrid microwave approach for phaseless imaging of dielectric targets," *IEEE Geosci. Remote Sens. Lett.*, vol. 12, no. 4, pp. 851–854, Apr. 2015, doi: 10.1109/LGRS.2014.2364077.
[71] G. Buonanno and R. Solimene, "Large linear random symmetric arrays," *Prog. Electromagn. Res. M*, vol. 52, pp. 67–77, 2016.
[72] G. Buonanno and R. Solimene, "Comparing different schemes for random arrays," *Prog. Electromagn. Res. B*, vol. 71, pp. 107–118, 2016.
[73] G. Buonanno and R. Solimene, "Generalised random binned antenna arrays," *Prog. Electromagn. Res. C*, vol. 78, pp. 129–143, 2017.
[74] G. Buonanno and R. Solimene, "Unequally-excited linear totally random antenna arrays for multi-beam patterns," *IET Microw., Antennas Propag.*, vol. 12, no. 10, pp. 1671–1678, Aug. 2018.
[75] G. Buonanno and R. Solimene, "Global characterization of linear statistically thinned antenna arrays," *IEEE Access*, vol. 9, pp. 119629–119640, 2021.
[76] G. Buonanno, S. Costanzo, and R. Solimene, "Statistically thinned array antennas for simultaneous multibeam applications," *IEEE Access*, vol. 10, pp. 60230–60240, 2022.
[77] G. Buonanno, S. Costanzo, and R. Solimene, "Broadband statistically designed thinned-binned array antennas," *IEEE Trans. Antennas Propag.*, vol. 71, no. 3, pp. 2454–2466, Mar. 2023.

FRANCESCA VENNERI (Member, IEEE) received the degree in information technology engineering from the Università della Calabria, Italy, in 1998, and the Ph.D. degree in electronic engineering from the Università Mediterranea di Reggio Calabria, in 2002. She is currently an Assistant Professor with the Università della Calabria. Her research interests include microstrip reflectarrays, antenna analysis and synthesis, RFID technology, metamaterial absorbers, and RF energy harvesting. She is a member of the IEEE Antennas and Propagation Society, the Società Italiana di Elettromagnetismo (SIEm), and the Consorzio Nazionale Interuniversitario per le Telecomunicazioni (CNIT).

SANDRA COSTANZO (Senior Member, IEEE) received the Laurea degree (summa cum laude) in computer engineering from the Università della Calabria, Rende, Italy, in 1996, and the Ph.D. degree in electronic engineering from the Università Mediterranea di Reggio Calabria, Reggio Calabria, Italy, in 2000.

She is currently a Full Professor in electromagnetic fields with the Università della Calabria, where she is also a Rector's Delegate for Health Safety. She teaches courses on electromagnetic waves propagation, antennas, remote sensing, radar, sensors, and electromagnetic diagnostics. She has authored or coauthored more than 230 contributions in international journals, books, and conferences. Her research interests include near-field/far-field techniques, antenna measurement techniques, antenna analysis and synthesis, numerical methods in electromagnetics, millimeter wave antennas, reflectarrays, synthesis methods for microwave structures, electromagnetic characterization of materials, biomedical applications, and radar technologies.

Dr. Costanzo is a member of the IEEE South Italy Geoscience and Remote Sensing Chapter, the Consorzio Nazionale Interuniversitario per le Telecomunicazioni (CNIT), the Società Italiana di Elettromagnetismo (SIEM), and the Centro Interuniversitario sulle Interazioni fra Campi Elettromagnetici e Biosistemi (ICEMB); a Board Member of the IEEE AP/ED/MTT North Italy Chapter; and the Vice-Chair of the IEEE MTT-28 Biological Effects and Medical Applications Committee. She received the Telecom Prize for the Best Laurea Thesis, in 1996, and the Best Academia and Research Application in Aerospace and Defense 2013 Award for the Application Software Defined Radar Using the NI USRP 2920 Platform. She is an Associate Editor Emeritus of IEEE JOURNAL OF ELECTROMAGNETICS, RF AND MICROWAVES IN MEDICINE AND BIOLOGY; an Associate Editor of IEEE ACCESS; a Section Editor of *Sensors* (section Physical Sensors), *Electronics* (section Microwave and Wireless Communications), and *Polymers* (section Smart and Functional Polymers Section); an Editorial Board Member of *Radioengineering* and *International Journal of RF and Microwave Computer-Aided Engineering*. She is an Editor of the books titled *Microwave Materials Characterization* (INTECH, 2012) and *Wave Propagation Concepts for Near-Future Telecommunication Systems* (INTECH, 2017). She is a lead editor of more than 12 special issues on international journals.

ANTONIO BORGIA (Member, IEEE) was born in Reggio Calabria, Italy. He received the Laurea degree in computer engineering and the Ph.D. degree in system and computer engineering from the Università della Calabria, in 2008 and 2013, respectively. He has (co)authored more than 50 contributions in international journals and conferences. His research interests include millimeter-wave antennas and technologies, printed antennas, and reflectarrays. He is a member of the Consorzio Nazionale Interuniversitario per le Telecomunicazioni (CNIT), Centro Nazionale di Ricerca Interuniversitario sulla Interazione fra Campi Elettromagnetici e Biosistemi (ICEmB), and Società Italiana di Elettromagnetismo (SIEm).

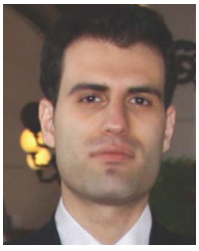

GIOVANNI BUONANNO (Member, IEEE) received the M.S. degree (summa cum laude) in electronic engineering from the Seconda Università degli Studi di Napoli (SUN), Aversa, Italy, in 2014, and the Ph.D. degree in industrial and information engineering from the University of Campania, in 2018. Then, he joined the Research Group in Applied Electromagnetics of SUN. He defending his Ph.D. thesis, in January 2019. Since 2022, he has been collaborating with the ElectRomagnetics MIcrowaves and Antennas for Sensing and Diagnostics Laboratory, Università della Calabria. His research interests include analysis and design of non-uniformly-spaced antenna arrays, biomedical applications, signal processing, and machine learning.

Open Access funding provided by 'Università della Calabria' within the CRUI CARE Agreement